Transactions of Materials Research 1 (2025) 100006

Contents lists available at ScienceDirect

Transactions of Materials Research

journal homepage: www.sciencedirect.com/journal/transactions-of-materials-research

Nickel carrier transfer bridge for improved photocatalytic water splitting of Zn_2GeO_4

Ruiqing Zou [a,b], Sibi Liu [a,b], Jie Su [c], Weiheng Ding [a,b], Yijin Wang [a,b], Fei Yan [a,b], Peng Guo [a,b], Junchao Zhou [a,b], Youzi Zhang [a,b], Xuanhua Li [a,b,*]

[a] State Key Laboratory of Solidification Processing, Center for Nano Energy Materials, School of Materials Science and Engineering, Northwestern Polytechnical University, Xi'an, 710072, China
[b] Research and Development Institute of Northwestern Polytechnical University, Shenzhen, 518057, China
[c] State Key Discipline Laboratory of Wide Band Gap Semiconductor Technology, Shaanxi Joint Key Laboratory of Graphene School of Microelectronics, Xidian University, Xi'an, 710071, China

ARTICLE INFO

Keywords:
Photocatalytic hydrogen evolution
Zn_2GeO_4
Metal-nickel bridging
Charge separation
Interface matching

ABSTRACT

Photocatalytic water splitting can convert solar energy into hydrogen, which has important implications for reducing dependence on fossil fuels. Constructing heterojunctions is a universal method for facilitating charge transfer, but the poor interface matching limits its charge separation and photocatalytic activity. Here, a metal-nickel bridging (nickel interlayer) NiO-Ni-Zn_2GeO_4 photocatalyst with well interface matching is designed through a partial oxidation strategy. Structure and *in situ* Raman characterization demonstrate that the nickel interlayer substantially optimizes interface matching and causes the first-order phonon mode transfer from the first-order longitudinal wave to the first-order transverse wave, which implies that NiO acts as the site for hydrogen production and violent surface reaction. Therefore, the nickel interlayer provides a charge transfer channel for carrier separation. Meanwhile, density functional theory calculations prove an optimal hydrogen-oxygen bond-breaking process with 36 % barriers decrease obtained via the effect of nickel interlayer. As a result, NiO-Ni-Zn_2GeO_4 shows the photocatalytic hydrogen production rate of 206.6 μmol g^{-1} h^{-1}, which is over 8 times greater than that of Zn_2GeO_4. This study offers a new approach for designing heterojunctions with well-matched interface and efficient charge separation.

1. Introduction

Photocatalytic water splitting to hydrogen (H_2) is considered the most efficient means of resolving the present global energy and environmental crisis. In recent years, metal oxides have emerged as promising photocatalysts due to their stability, abundant availability, and non-toxicity, making them widely used in photocatalytic water splitting applications [1–3]. Among typical metal oxides [4–6], Zn_2GeO_4 (ZGO) is a promising photocatalytic material because of its high carrier mobility and conductivity [7–9]. However, severe carrier recombination limits photocatalytic performance of individual ZGO [10–12].

The construction of ZGO-based heterojunctions is thought of as an effective way to increase carrier separation and photocatalytic activity. For instance, monometallic cocatalysts, e.g., gold (Au), platinum (Pt), silver (Ag) [13–15] and base metals such as nickel (Ni) and iron (Fe), are commonly used to improve photocatalytic performance via providing active sites for surface reactions and enhancing carrier migration efficiency [16–18]. In addition, integrating ZGO with energy band structure matching semiconductors can induce the directional transfer of photogenerated carriers and facilitate charge separation [19], which have also been widely used to boost catalytic activity [20–22]. Wang et al. enhanced the photocatalytic H_2 production performance of ZGO by constructing ZGO/ZnS intimate heterojunction [13]. Hou et al. enhanced the photoinduced carriers' separation and transfer efficiency in ZGO by combining it with CdS, thereby boosting its photocatalytic performance [23]. Hou et al. further reported that by re-conjugating ZGO to ZnO (heterojunction) and depositing metals (Cu, monometallic cocatalysts) on the surface, ZnO/Zn_2GeO_4-Cu exhibited enhanced light absorption and prevented electron-hole pair recombination, which greatly promoted the photocatalytic performance [24]. However, the limited interface

* Corresponding author. State Key Laboratory of Solidification Processing, Center for Nano Energy Materials, School of Materials Science and Engineering, Northwestern Polytechnical University, Xi'an, 710072, China.
E-mail address: lixh32@nwpu.edu.cn (X. Li).

https://doi.org/10.1016/j.tramat.2025.100006
Received 22 March 2025; Received in revised form 2 April 2025; Accepted 2 April 2025
Available online 5 April 2025

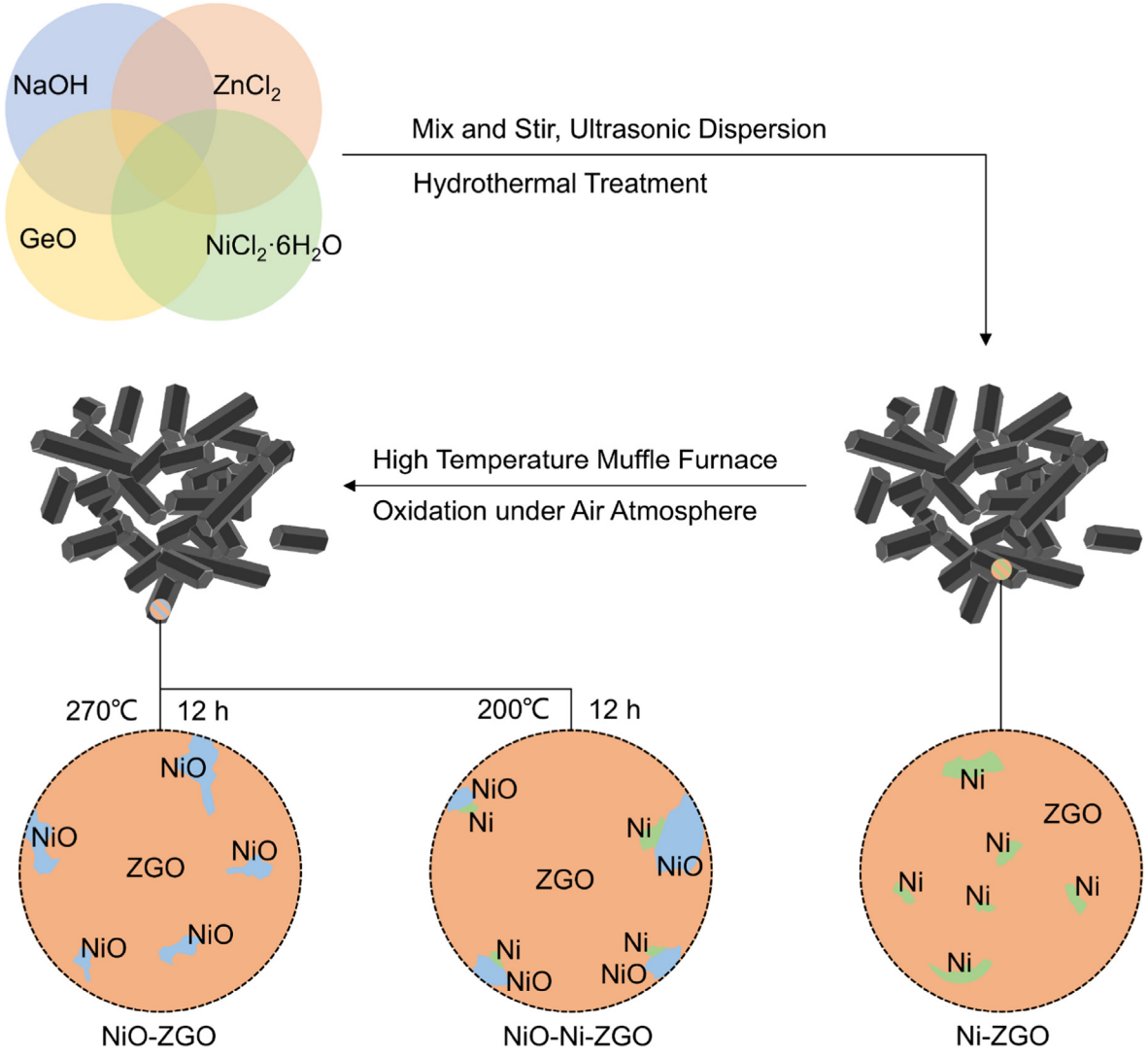

Fig. 1. Synthesis of the Ni-ZGO, NiO-Ni-ZGO and NiO-ZGO nanorods.

matching in ZGO-based heterojunctions continues to result in substantial carrier recombination [25–27]. Therefore, developing a ZGO heterojunction photocatalyst with a well-matched interface remains a key scientific challenge for efficient photocatalytic water splitting.

In this study, we construct a metal-nickel bridging (nickel interlayer) NiO-Ni- ZGO photocatalyst through the partial oxidation strategy. The partial oxidation of NiO from Ni generates a well-matched interface between ZGO and NiO, while the unoxidized Ni serves as a carrier migration bridge to facilitate photogenerated carriers transfer and separation. The synergistic change of the first-order phonon mode with the hydroxyl group (water) in the *in situ* Raman characterization reveals that, in the NiO-Ni-ZGO, NiO acts as the site for hydrogen production, while ZGO primarily provides carriers. In addition, the metal-nickel interlayer significantly reduces the photoinduced carrier transfer resistance and obtains barrier decrease during photocatalytic H_2 evolution process. As a result, NiO-Ni-ZGO exhibits a lot of increase in photocatalytic H_2 evolution compared with single ZGO, outperforming previously reported ZGO-based photocatalyst.

2. Experimental procedures

2.1. Reagents

Germanium oxide (GeO_2, 99.99 % metal basis), zinc chloride ($ZnCl_2$, 98 % AR), and sodium hydroxide (NaOH, 96 %) were purchased from MACKLIN (Shanghai Macklin Biochemical Co., Ltd). Nickel chloride hexahydrate ($NiCl_2{\cdot}6H_2O$, 99 % AR) was purchased from RHAWN. All chemicals were used as received without further purification. Deionized water (~18.25 MΩ cm) was used throughout this study.

2.2. Methods

2.2.1. Synthesis of the Ni-ZGO nanorods

During a typical experiment, GeO_2, $ZnCl_2$, NaOH, and $NiCl_2{\cdot}6H_2O$ were added to 30 mL of water in turn, and their specific amounts are shown in Table S1. After 30 min of magnetic stirring, the mixture was transferred to a 50 mL Teflon-lined autoclave, where the reaction was sustained at 200 °C for 16 h and finally cooled naturally to room temperature. Next, the mixture was centrifuged twice each with water and absolute ethanol to completely remove residues and other impurities. The washed mixture was then fast vacuum dried in the oven at 80 °C for 24 h, where the product was dried completely, and their edges were coarsened.

2.2.2. Synthesis of the NiO-Ni-ZGO and NiO-ZGO nanorods

NiO-Ni-ZGO and NiO-Zn_2GeO_4 (NiO-ZGO) were obtained via further processing based on Ni-ZGO. In general, Ni-ZGO was heat treated in the muffle furnace at 200 °C, where NiO-Ni-ZGO was prepared, and 270 °C, where NiO-ZGO was formed, for 12 h, respectively (Fig. 1).

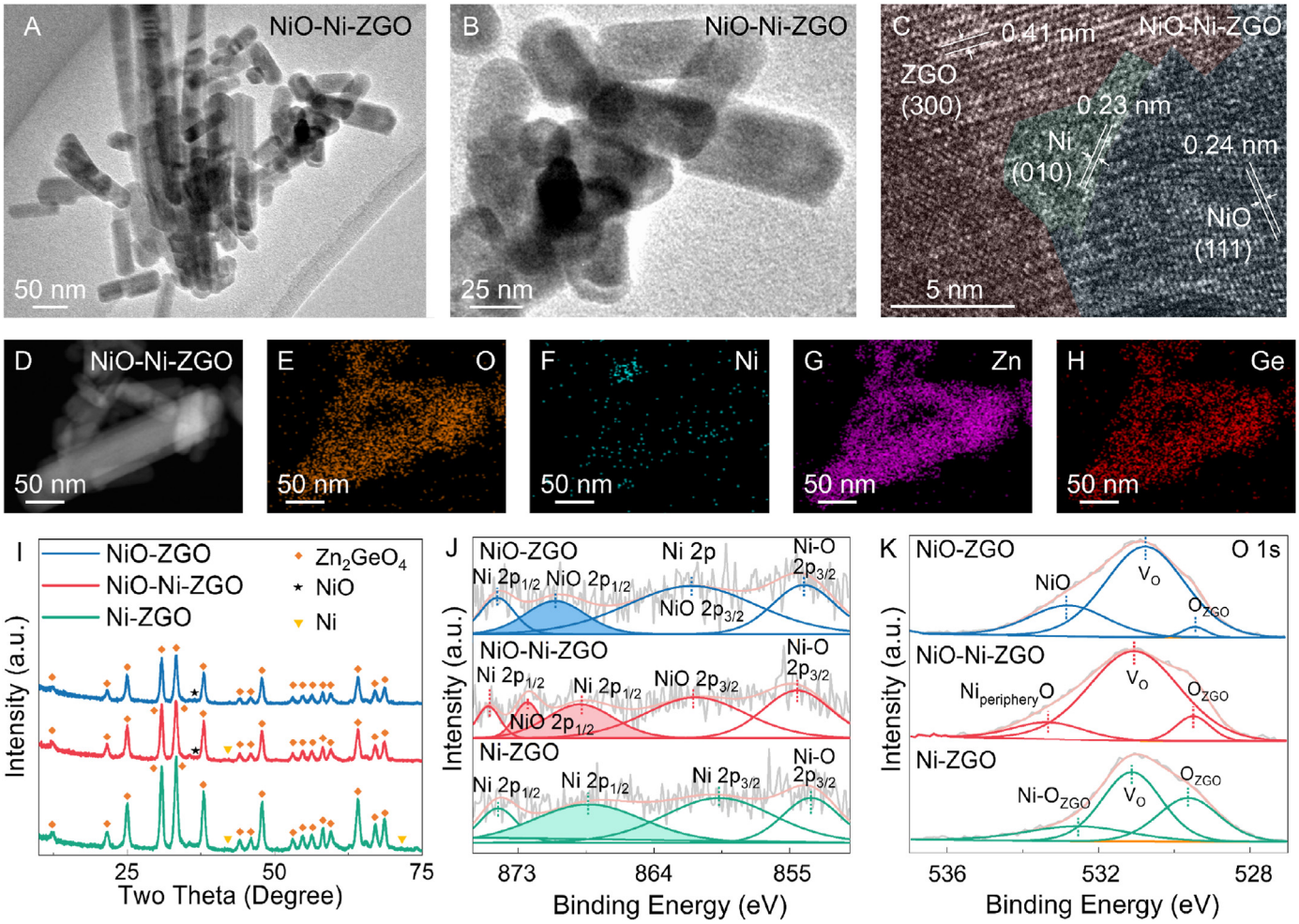

Fig. 2. Morphology and structure characterization of NiO-Ni-ZGO, NiO-ZGO and Ni-ZGO. (A) TEM image of NiO-Ni-ZGO and (B) the partial enlargement of A. (C) HRTEM image of NiO-Ni-ZGO. (D–H) TEM mapping of NiO-Ni-ZGO. (I) XRD pattern of NiO-Ni-ZGO, NiO-ZGO and Ni-ZGO. (J) Ni 2p spectra of NiO-Ni-ZGO, NiO-ZGO and Ni-ZGO, and (K) O 1s spectra of NiO-Ni-ZGO, NiO-ZGO and Ni-ZGO.

2.3. Characterization

Transmission electron microscopy (TEM) and high-resolution TEM (HRTEM) images were obtained by using FEI Tecnai G2 F20 (USA). TEM mapping images were performed with an EDAX Phoenix X-ray spectrometer (USA), and scanning electron microscope (SEM) images were characterized via Zeiss Sigma. X-ray diffraction (XRD) patterns were obtained from Kratos (XRD-7000) with Cu K_α ($\lambda = 1.54178$ Å) radiation to examine the chemical compositions in the scan range of 10-100° at the scanning speed of 3° per minute. The Raman spectra were measured via a RENISHAW Raman spectrometer in conjunction with a companion 532 nm laser. X-ray photoelectron spectroscopy (XPS) patterns were acquired on Kratos AXIS Ultra DLD, equipped with a monochromatized Al K_α ($h\nu = 1486.6$ eV) to characterize the chemical composition. Electrochemical impedance spectroscopy (EIS) patterns, Mott-Schottky (MS) plots (CHI-760E, CH Instruments Inc, USA), and amperometric current-time (*I-T*) curves (Zennium-E, ZAHNER, German) were carried out in a 0.5 M sodium sulfate solution at room temperature with a classical three-electrode system containing a platinum plate as a counter electrode, a silver chloride reference electrode, and the sample as the working electrode (AM 1.5 G Xe lamp). Before the test, the sample was immersed in sodium sulfate solution for a period to obtain stable open-circuit potential. Photoluminescence (PL) spectra were examined via a PL spectrometer (FLS 980) and the excitation wavelength was 294 nm. Time-resolution photoluminescence (TR-PL) spectrum was examined via the FLS920 fluorescence spectrometer (Edinburgh Instruments) and the emission wavelength was 530.5 nm. UV–vis diffuse reflectance spectroscopy (UV–VIS-DRS) patterns were measured on PerkinElmer LAMBDA 850+.

2.4. Photocatalytic water splitting measurements

The photocatalytic water splitting measurements were conducted in a sealed online reactor (Perfectlight Limited, China). In a general process, 10 mg prepared powder samples were dispersed in 45 mL water, followed by 5 mL of methanol (AR) and 1.55 μL 8 wt% chloroplatinic acid solution dropwise with ultrasonication and continue for a period until homogeneous. The dispersed solution was then poured into the reactor, and the vacuum began immediately after the reactor was installed until the barometer had shown stability. The light irradiation was provided via a PLS-SXE300 Xe lamp (Perfectlight Limited, China) with a standard AM 1.5 G filter, which could output about 100 mW cm^{-2} light density and was calibrated by an optical power meter. Using high-purity nitrogen as the carrier gas, we qualitatively detected the hydrogen produced by decomposition with GC-2014C (SHIMADZU, Japan) gas chromatograph equipped with column and thermal conductivity detector (TCD) for more than 6 h in each test.

2.5. In situ Raman characterization

In a typical *in situ* Raman characterization, 10 mg prepared powder samples were dispersed in 45 mL water, followed by 5 mL of methanol

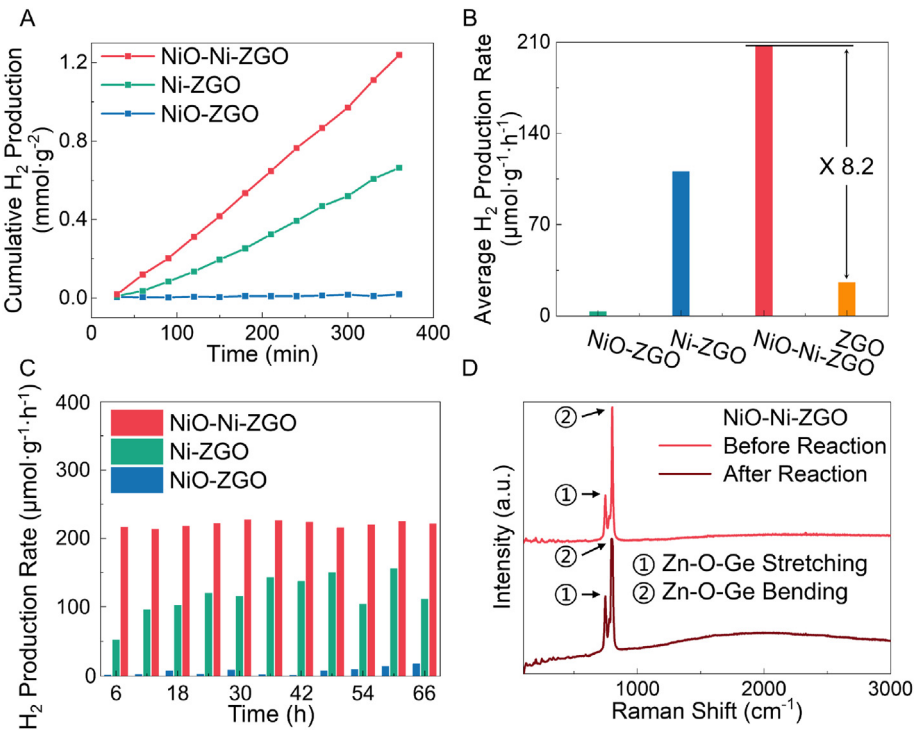

Fig. 3. Performance of photocatalytic water splitting to produce hydrogen via NiO-Ni-ZGO, Ni-ZGO, and NiO-ZGO. (A) Cumulative hydrogen production under long-term test conditions of NiO-Ni-ZGO (red), Ni-ZGO (green), and NiO-ZGO (blue). (B) Average hydrogen production rate of NiO-Ni-ZGO (red), Ni-ZGO (green), NiO-ZGO (blue), and ZGO (orange). (C) Hydrogen production during the 6-h cycle of NiO-Ni-ZGO (red), Ni-ZGO (green) and NiO-ZGO (blue). (D) Raman spectra of NiO-Ni-ZGO before and after reaction.

(AR) with ultrasonication, and continued for a time interval until homogeneous. A certain amount of the above mixture solution was dropwise in a sandwich reaction system consisting of two slides, which were then placed flat on the stage. The choice of the illumination system was consistent with that of photocatalytic water splitting measurements. Raman measurements were conducted using an inVia (RENISHAW, UK) Raman detector. It should be noted that the illumination system should be kept at a distance from the sandwich reaction system, and the path of light should be parallel to the slide, in other words, perpendicular to the Raman laser (532 nm, RL532C50, RENISHAW, UK), which must be maintained maximum strength during the whole characterization.

3. Results

3.1. Catalyst synthesis and characterization

For preparation of the NiO-Ni-ZGO heterojunction photocatalyst, a two-step procedure was adopted (Fig. 1). Initially, the basic ZGO containing metal Ni (Ni-ZGO) was synthesized by sodium hydroxide-assisted hydrothermal co-deposition. Subsequently, the surface Ni metal was partially oxidized via thermal oxidation to form NiO-Ni-ZGO (details in the methods section). Both ZGO and Ni-ZGO displayed a nanorod structure, as clearly shown in Fig. S1. NiO-Ni-ZGO exhibited a multi-prism morphology with regular geometry as evidenced by transmission electron microscopy (TEM) images (Fig. 2A and B). Meanwhile, high-resolution transmission electron microscopy (HRTEM) images of NiO-Ni-ZGO revealed lattice fringes of 0.23, 0.24, and 0.41 nm, which could be attributed to the (010), (111), and (300) lattice planes of Ni, NiO, and ZGO, respectively, demonstrating the successful formation of NiO-Ni-ZGO (Fig. 2C) [5,10]. Notably, Ni was surrounded similarly to a bridge and wrapped up via both ZGO and NiO. Fig. 2D–H presents the TEM mapping diagrams of the sample, where the elements O, Zn, and Ge were evenly distributed. With further increase in the oxidation degree of Ni-ZGO, one could see that Ni-ZGO completely transformed into NiO-ZGO, where Ni disappeared, and only lattice fringes for NiO and ZGO could be observed (Figs. S2 and S3). The X-ray diffraction patterns of Ni-ZGO, NiO-Ni-ZGO, or NiO-ZGO only exhibited the characterization peaks of Zn_2GeO_4 (JCPDS No. 11–0687), which could be ascribed to the low content of Ni (Fig. 2I) [5,9].

We further investigated the detailed interfacial interactions of NiO-Ni-ZGO. X-ray photoelectron spectroscopy (XPS) is an efficient method to study the interfacial electronic structure among Ni-ZGO, NiO-Ni-ZGO, and NiO-ZGO (Fig. 2J, K and Figs. S4A–D). At the beginning, four distinct Ni characteristic peaks were found in the Ni 2*p* XPS spectrum of Ni-ZGO, namely, the Ni $2p_{1/2}$ nickel containing characteristic peak located at 874.3 eV, the Ni $2p_{1/2}$ and Ni $2p_{3/2}$ nickel metal characteristic peaks located at 868.3 and 859.7 eV, and the Ni-O $2p_{3/2}$ nickel connected to ZGO characteristic peak located at 853.6 eV (Fig. 2J, green line) [5,28]. As oxidation progressed, NiO characteristic peaks of Ni $2p_{1/2}$ and Ni $2p_{3/2}$ located at 872.5 and 861.4 eV could be observed in the Ni 2*p* XP1S spectrum of NiO-Ni-ZGO, while the characteristic peak of nickel metal located at 867.8 eV indicated the existence of the Ni bridge wrapped up via both ZGO and NiO (Fig. 2J, red line) [28]. With further oxidation, a unique NiO $2p_{1/2}$ characteristic peak located at 870.5 eV appeared in the Ni 2*p* XPS spectrum of NiO-ZGO (Fig. 2J, blue line), which replaced the nickel metal characteristic peak in NiO-Ni-ZGO, indicating that Ni-ZGO was completely oxidized. Similarly to Ni 2*p*, the XPS spectra of O 1s were obtained. In Ni-ZGO, three distinct peaks appeared at 532.5, 531.1, and 529.6 eV, representing O (Ni-O_{ZGO}), vacancy oxygen (V_O), and material-O (O_{ZGO}), respectively (Fig. 2K, green line) [29]. As oxidation proceeds, it could be observed in NiO-Ni-ZGO that the O ($Ni_{periphery}O$) peak located at 533.3 eV appeared, ascribing to oxidation of the surface nickel metal (Fig. 2K, red line). As the oxidation further deepened, the O ($Ni_{periphery}O$) peak in NiO-Ni-ZGO split, forming the peak representing O (NiO) located at 532.8 eV (Fig. 2K, blue line) [5,29], which was due to complete oxidation so that the oxygen acting on nickel oxide was also associated with the metal in ZGO.

3.2. Photocatalytic hydrogen evolution performance

The photocatalytic hydrogen evolution of NiO-Ni-ZGO, NiO-ZGO, and Ni-ZGO under Xe lamp ($\lambda \geq 340$ nm, AM 1.5 G) with methanol (10 vol%) as sacrifice agent and platinum (8 wt%) as cocatalyst is shown in Fig. 3A. All three samples demonstrated linear and consistent hydrogen

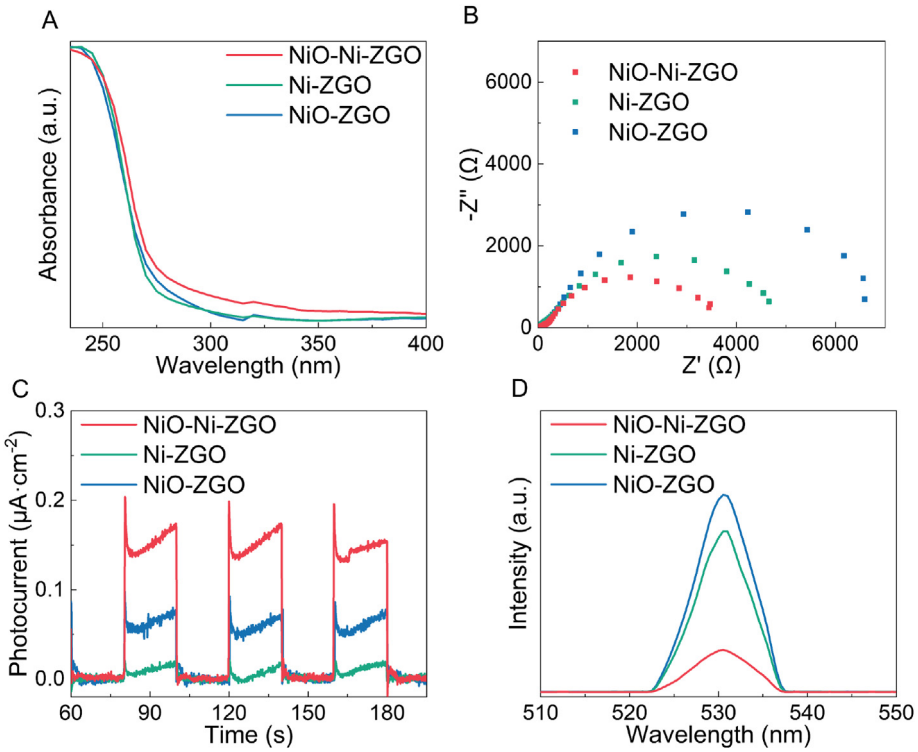

Fig. 4. Optical and electrochemical characterization of NiO-Ni-ZGO, Ni-ZGO, and NiO-ZGO. (A) UV–vis diffuse reflectance spectrum of NiO-Ni-ZGO, Ni-ZGO, and NiO-ZGO. (B) EIS Nyquist plots (the additional bias voltage was applied to cancel out the open-circuit voltage), and (C) photocurrent responses under the Xe lamp (AM 1.5 G) of NiO-Ni-ZGO, Ni-ZGO, and NiO-ZGO. (D) PL spectra excited at 295 nm of NiO-Ni-ZGO, Ni-ZGO, and NiO-ZGO.

production over time, indicating stable and reliable hydrogen evolution rates. The average hydrogen productivity of NiO-Ni-ZGO (206.625 μmol g^{-1} h^{-1}) was much higher than those of Ni-ZGO and NiO-ZGO (110.609 and 3.229 μmol g^{-1} h^{-1}), especially over 8 times that of ZGO (Fig. 3B, S5 and Table S2).

In addition, NiO-Ni-ZGO also exhibited good hydrogen production and structural stability. It maintained a hydrogen production rate consistently around 200 μmol g^{-1} during the 6-h cycle, with no significant decline, demonstrating its excellent resistance to photo-corrosion and environmental stability (Fig. 3C, red line). In contrast, NiO-ZGO exhibited negligible hydrogen production during the 6-h cycle (Fig. 3C, blue line). This was evident in long-term monitoring, where the production rate remained nearly constant and close to the X-axis (Fig. 3A, blue line), as well as in individual cycle monitoring, where fluctuations were minor and centered around the X-axis (Fig. 3C, blue line). In addition, the performance of Ni-ZGO was somewhere between NiO-Ni-ZGO and NiO-ZGO (Fig. 3A–C, green line). Fig. 3D shows the Raman spectra of NiO-Ni-ZGO before and after the reaction, where the peak region from 700 cm^{-1} to 850 cm^{-1} (Zn-O-Ge stretching around 750 cm^{-1}; Zn-O-Ge bending around 800 cm^{-1}) represented the characteristic peaks of ZGO. The peak region from 300 cm^{-1} to 600 cm^{-1} corresponding to NiO was almost invisible due to the low Ni content. No apparent change was observed in the Raman spectra of NiO-Ni-ZGO before and after the reaction, proving that the NiO-Ni-ZGO possessed excellent stability.

3.3. Optical and electrochemical performance

An important part of research on photocatalytic performance is optical and electrical characteristics of photocatalysts. The sample was evaluated for light absorption capacity by UV–VIS-DRS. NiO-Ni-ZGO exhibited a slight redshift and stronger degree absorption compared to Ni-ZGO and NiO-ZGO (Fig. 4A). Fig. 4B illustrates the electrocatalytic impedance spectra (EIS) of these materials, showing that NiO-Ni-ZGO exhibited the lowest impedance due to the Ni bridging, indicating superior conductivity. This result confirmed that NiO-Ni-ZGO's good interface matching significantly enhanced carrier transfer efficiency. This was further evidenced in Fig. 4C, where NiO-Ni-ZGO demonstrated both the highest photocurrent densities.

The charge separation efficiency was calculated to be 69.7 % for the NiO-Ni-ZGO sample (see Note 1 in Supporting information). In addition, the photoluminescence spectroscopy (PL) shows that the lowest PL intensity of NiO-Ni-ZGO, compared with NiO-ZGO and Ni-ZGO, proving the highest carrier separation efficiency in NiO-Ni-ZGO (Fig. 4D). Furthermore, the charge separation kinetics of these materials was detected by time-resolved photoluminescence spectroscopy (TR-PL), where the lifetime (τ) of NiO-Ni-ZGO were 2.930 ns, close to 2 and 8 times higher than that of NiO-ZGO (1.881 ns) and Ni-ZGO (0.392 ns) (Fig. S6). This demonstrates the excellent interfacial carrier pass-through efficiency of NiO-Ni-ZGO. Its superior interface matching significantly enhances carrier capture and consequently improves decomposition efficiency.

3.4. *In situ* Raman study

The *in situ* Raman spectra were conducted to elucidate charge migration kinetic during the photocatalytic process (Fig. 5). In *in situ* Raman, the photocatalytic reaction solution was sandwiched between two slides, with the Raman laser perpendicular to the slides and the Xe lamp (AM 1.5 G) parallel to the slides. The Raman peak region from 700 cm^{-1} to 850 cm^{-1} (Zn-O-Ge stretching around 750 cm^{-1}; Zn-O-Ge bending around 800 cm^{-1}) represented the characteristic peaks of ZGO (Fig. S7), and the region of 300–600 cm^{-1} corresponds to the first-order phonon modes of Ni-O, whereas the range of 300–450 cm^{-1} was the first-order transverse wave region of Ni-O (1TO), and the range of 450–600 cm^{-1} was the first-order longitudinal wave region of Ni-O (1LO) (Fig. 5A1, B1, C1) [30]. After the reaction began, unlike the 1LO declined only in Ni-ZGO and the 1TO declined only in NiO-ZGO, the vibration

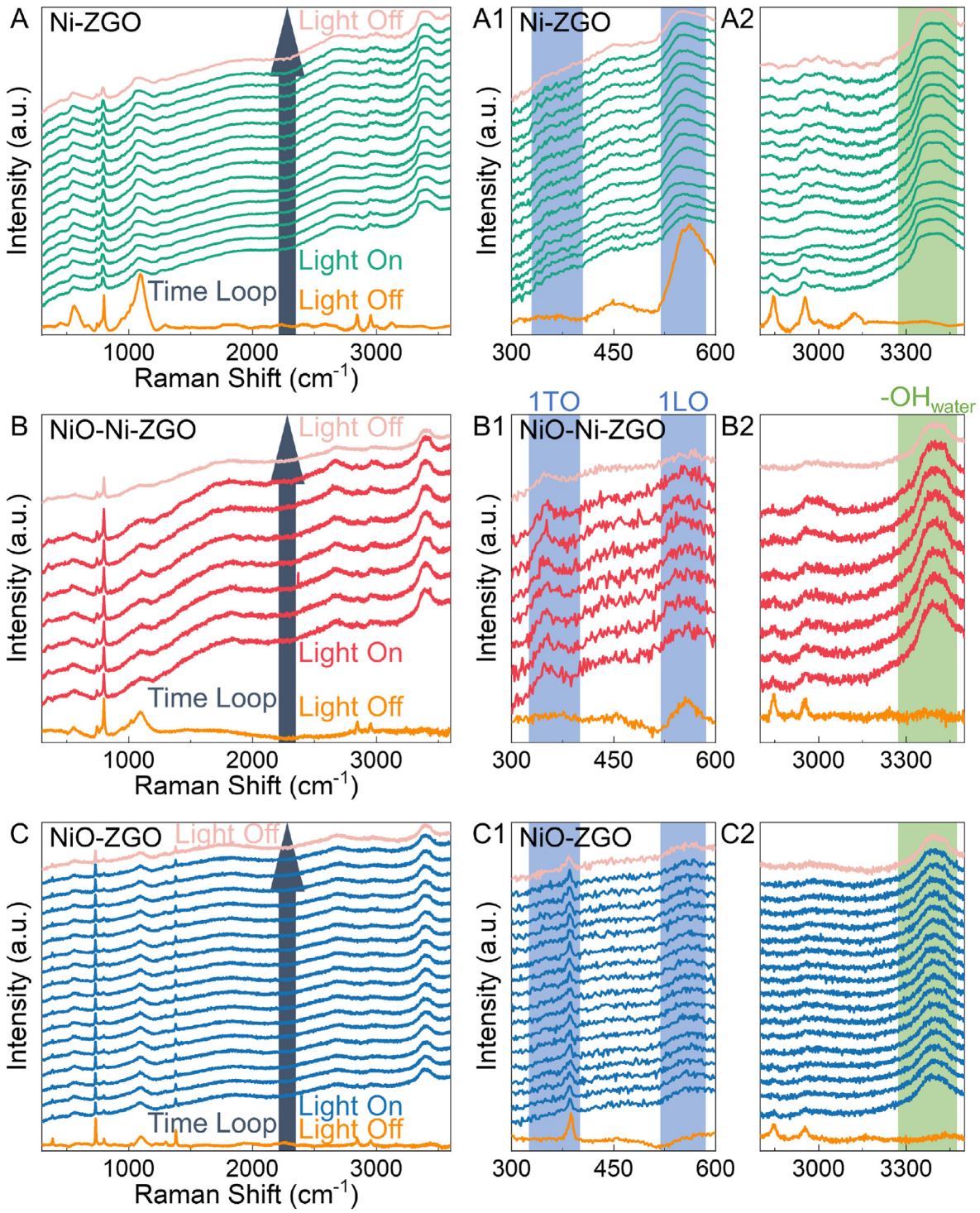

Fig. 5. *In situ* Raman characterization and experimental mechanism studies, i.e., *in situ* Raman full spectra of Ni-ZGO (A), NiO-Ni-ZGO (B), and NiO-ZGO (C). (A1, B1, C1) and (A2, B2, C2) were locally amplified *in situ* Raman spectra of (A, B, C), respectively. The orange lines indicated when the light had not been turned on, and the light pink lines indicated when the light had just been turned off. When illuminated, the interval between the two lines was 5 min. The Raman laser was 532 nm.

mode of first-order phonons in NiO-Ni-ZGO changed from 1LO to 1TO, which indicates that a large and obvious energy change (giving and dissipating) occurred only on the surface of NiO-Ni-ZGO during the photocatalysis process [7,30]. Therefore, NiO of NiO-Ni-ZGO was the site for hydrogen production. Meanwhile, we also observed the characteristic peak region of hydroxyl group (-OH_{Water}) of water at 3300-3600 cm^{-1}, with significant variations in peak intensity, indicating that water molecules were split via photocatalyst and left -OH_{Water} (Fig. 5A2, B2, C2), which was the key precondition for hydrogen to be produced [7]. The energy change represented by the change in the first-order phonon (from 1LO to 1TO) pattern was used by the free hydrogen ions (H^+ $_{Water}$, corresponding to -OH_{Water}) to aggregate around the NiO and produce hydrogen. Therefore, from the perspective of *in situ* Raman, the presence of Ni bridge in NiO-Ni-ZGO enabled it to have better peak characteristics during the photocatalysis process, and carriers to shuttle between NiO and ZGO more efficiently and participate in a large number of reactions

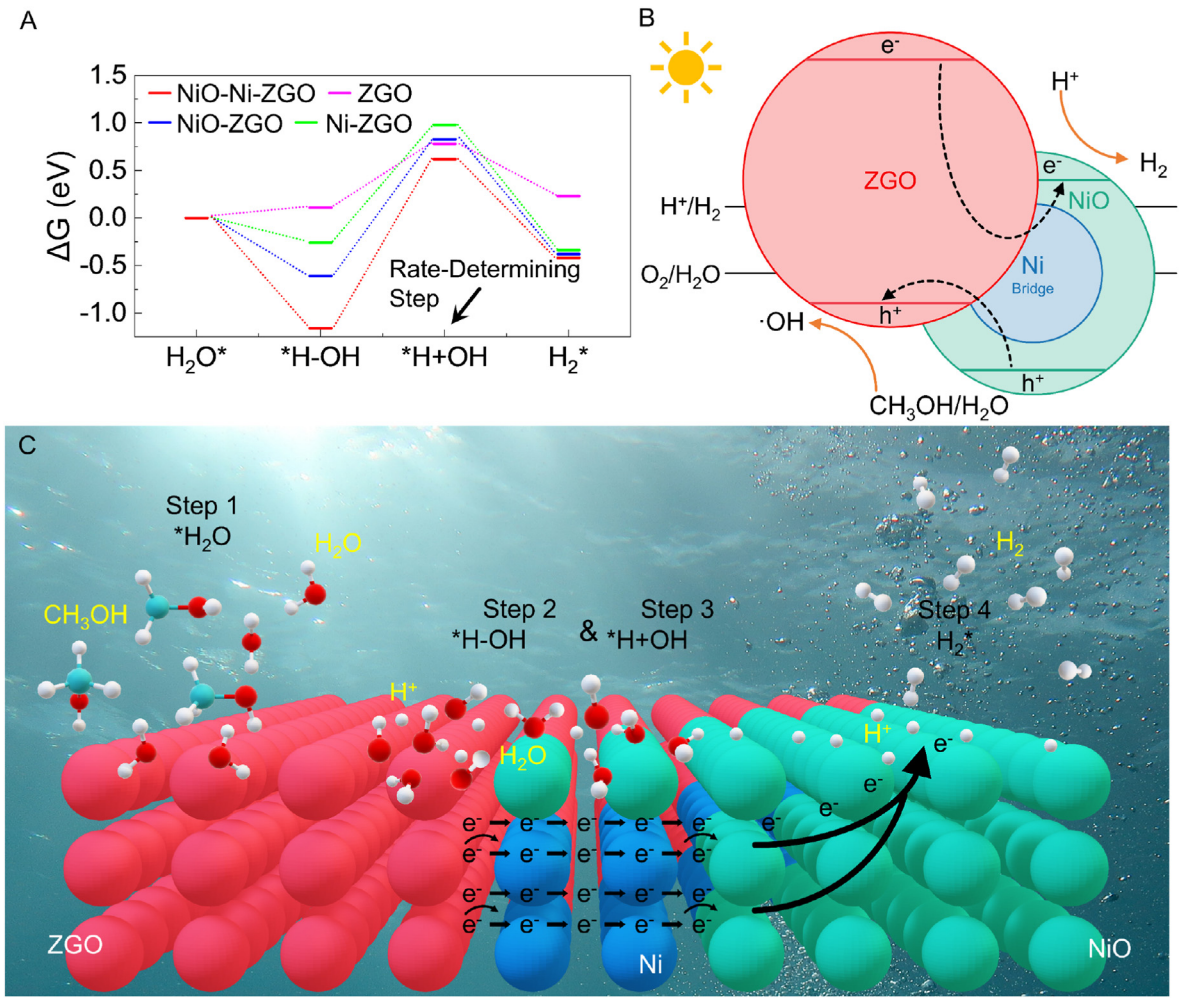

Fig. 6. Density functional theory calculations and the possible photocatalytic reaction mechanism of photocatalytic water splitting to produce hydrogen. (A) Free energy diagram of photocatalytic water splitting to produce hydrogen on the surface of ZGO, Ni-ZGO, NiO-ZGO, and NiO-Ni-ZGO. (B) The possible optimization of Ni as the "bridge" in the band structure. (C) Possible reaction process of photocatalytic hydrogen production on the surface of NiO-Ni-ZGO, where nickel acted as the bridge to efficiently transfer carriers, the red, blue, and green areas represented ZGO, Ni, and NiO, respectively.

on the surface. The presence of Ni bridge greatly improved the carrier migration efficiency.

3.5. Reaction mechanism

The photocatalytic H_2 evolution process and the corresponding Gibbs free energy were further calculated via density functional theory (DFT) (Fig. 6A). In this study, photocatalytic water splitting could be divided into four steps from the point of view of water molecules [31–33]. The 1st step was the contact between water molecules with the surface of material. The 2nd step was to transfer photogenerated carriers to the hydrogen ion endpoint. The 3rd step was to strip the hydrogen ion, i.e., the hydrogen-oxygen (H-O) bond breaking. The 4th step was the generation of hydrogen. These 4 steps correspond to the $*H_2O$, *H-OH, *H + OH, and H_2* steps, as shown in Fig. S8 [34]. The rate determining step (RDS) of ZGO-based photocatalytic process was the H-O bond-breaking step after carrier migration. At the RDS, NiO-Ni-ZGO exhibited a lower energy barrier with the value of 0.62 eV, which was 20.5 %, 25.3 %, and 36.7 % lower than those of ZGO, NiO-ZGO, and Ni-ZGO. This indicates that the Ni layer optimized the electronic structure of Ni-NiO, which made NiO a more efficient active site for photocatalytic H_2 evolution.

To characterize the conduction band (CB) position of the material, the Mott-Schottky test was performed, and the results are shown in Fig. S9. By extrapolating the tangents of the Mott-Schottky curves recorded at various frequencies, the intersection points on the X-axis could be determined. The conduction bands of ZGO and NiO were −1.90 and −0.63 eV (vs. Reversible Hydrogen Electrode, RHE), respectively. In combination with the above characterization, a possible carrier migration process of NiO-Ni-ZGO was depicted in Fig. 6B, where ZGO and NiO both crossed the band gap required to photocatalytic water splitting well (vs. RHE, Fig. S10). Compared with NiO-ZGO and Ni-ZGO (Figs. S11A and B), Ni bridge, as the charge transfer channel, improved the carrier separation and migration efficiency in NiO-Ni-ZGO (Fig. 6B), resulting in a more intense and efficient photocatalytic reaction on the surface of NiO-Ni-ZGO, which was also confirmed by the conversion of first-order phonon vibration mode from 1LO to 1TO (Fig. 5B1).

Therefore, combined with the RDS results and band structure, a feasible hydrogen production mechanization could be illustrated (Fig. 6C). Under light irradiation, photogenerated electrons and holes were simultaneously excited on both the CB and the VB of the NiO part and the ZGO part of the NiO-Ni-ZGO. Then, benefitted from the Ni bridging as charge transfer channel, the photoinduced electrons migrated from CB of ZGO to Ni, then accumulated at CB of NiO for H_2 evolution. Meanwhile, the photoinduced holes at VB of NiO transferred through the Ni bridging to VB of ZGO and consumed by sacrifice agent CH_3OH. The Ni bridging successfully optimized the contact matching between NiO and ZGO, promoting charge separation, whereas electronic structure of Ni-NiO was also modified and lowered H-O bond-breaking barrier,

resulting in great increase in photocatalytic activity.

4. Conclusion

In conclusion, we designed a partial oxidation strategy to obtain a NiO-Ni-ZGO heterojunction photocatalytic material with the interfacial metal Ni as an electron transfer bridge. Compared to ZGO, Ni-ZGO and NiO-ZGO, NiO-Ni-ZGO exhibited superior photoelectrochemical performance, with hydrogen production rates increasing by over 8 times (206.6 μmol g^{-1} h^{-1}) and demonstrated excellent stability (66 h). The *in situ* Raman characterization revealed that the metal nickel interlayer acts as an effective bridge, which enhanced the carrier flow efficiency. DFT calculations pointed out that the presence of metal nickel could reduce the energy requirement up to more than 36 % at the critical step of the reaction. This study provided a new idea for improving the heterojunction with a poor matching degree and realizing the efficient ZGO photocatalytic water splitting to produce hydrogen.

CRediT authorship contribution statement

Ruiqing Zou: Writing – original draft. **Sibi Liu:** Writing – review & editing. **Jie Su:** Software. **Weiheng Ding:** Writing – review & editing. **Yijin Wang:** Writing – review & editing. **Fei Yan:** Writing – review & editing. **Peng Guo:** Writing – review & editing. **Junchao Zhou:** Writing – review & editing. **Youzi Zhang:** Writing – review & editing. **Xuanhua Li:** Writing – review & editing.

Data availability

The authors declare that the data supporting the findings of this study are available within the article and its Supplementary Information files.

Declaration of competing interest

The authors declare that they have no known competing financial interests or personal relationships that could have appeared to influence the work reported in this paper.

Acknowledgments

This research is supported by the Science, Technology, and Innovation Commission of Shenzhen Municipality (JCYJ20220818103417036), the National Natural Science Foundation of China (22261142666), the Fundamental Research Funds for the Central Universities, the China National Postdoctoral Program for Innovative Talents (BX20230496, BX20240490), the Youth Talent Support Program of Shaanxi Province (20240463).

Appendix A. Supplementary data

Supplementary data to this article can be found online at https://doi.org/10.1016/j.tramat.2025.100006.

References

[1] J. Zhu, W. Shao, X. Li, X. Jiao, J. Zhu, Y. Sun, Y. Xie, Asymmetric triple-atom sites confined in ternary oxide enabling selective CO_2 photothermal reduction to acetate, J. Am. Chem. Soc. 143 (2021) 18233–18241, https://doi.org/10.1021/jacs.1c08033.

[2] W. Chong, B. Ng, L. Tan, S. Chai, A compendium of all-in-one solar-driven water splitting using $ZnIn_2S_4$-based photocatalysts: guiding the path from the past to the limitless future, Chem. Soc. Rev. 53 (2024) 10080–10146, https://doi.org/10.1039/D3CS01040F.

[3] Z. Ma, B. Guan, J. Guo, X. Wu, Y. Chen, J. Zhang, X. Jiang, S. Bao, L. Chen, K. Shu, H. Dang, Z. Guo, Z. Li, S. Yao, Z. Huang, State of the art and prospectives of heterogeneous photocatalysts based on metal–organic frameworks (MOFs): design, modification strategies, and their applications and mechanisms in photodegradation, water splitting, and CO_2 reduction, Catal. Sci. Technol. 13 (2023) 4285–4347, https://doi.org/10.1039/D3CY00479A.

[4] J. Liang, J. Xu, Q. Gu, Y. Zhou, C. Huang, H. Lin, X. Wang, A novel Zn_2GeO_4 superstructure for effective photocatalytic hydrogen generation, J. Mater. Chem. A 1 (2013) 7798–7805, https://doi.org/10.1039/C3TA11374D.

[5] J. Huang, K. Ding, Y. Hou, X. Wang, X. Fu, Synthesis and photocatalytic activity of Zn_2GeO_4 nanorods for the degradation of organic pollutants in water, ChemSusChem 1 (2008) 1011–1019, https://doi.org/10.1002/cssc.200800166.

[6] G. Zhao, X. Xu, Cocatalysts from types, preparation to applications in the field of photocatalysis, Nanoscale 13 (2021) 10649–10667, https://doi.org/10.1039/D1NR02464G.

[7] Y. Wang, S. Zheng, W. Yang, R. Zhou, Q. He, P. Radjenovic, J. Dong, S. Li, J. Zheng, Z. Yang, G. Attard, F. Pan, Z. Tian, J. Li, *In situ* Raman spectroscopy reveals the structure and dissociation of interfacial water, Nature 600 (2021) 81–85, https://doi.org/10.1038/s41586-021-04068-z.

[8] Q. Liu, Y. Zhou, J. Kou, X. Chen, Z. Tian, J. Gao, S. Yan, Z. Zou, High-yield synthesis of ultralong and ultrathin Zn_2GeO_4 nanoribbons toward improved photocatalytic reduction of CO_2 into renewable hydrocarbon fuel, J. Am. Chem. Soc. 132 (2010) 14385–14387, https://doi.org/10.1021/ja1068596.

[9] Q. Liu, L. Zhang, P. Crozier, Structure-reactivity relationships of Ni-NiO core-shell co-catalysts on Ta_2O_5 for solar hydrogen production, Appl. Catal. B Environ. 172 (2015) 58–64, https://doi.org/10.1016/j.apcatb.2015.01.008.

[10] J. Liang, Y. Cao, H. Lin, Z. Zhang, C. Huang, X. Wang, A template-free solution route for the synthesis of well-formed one-dimensional Zn_2GeO_4 nanocrystals and its photocatalytic behavior, Inorg. Chem. 52 (2013) 6916–6922, https://doi.org/10.1021/ic302698z.

[11] J. Sato, H. Kobayashi, K. Ikarashi, N. Saito, H. Nishiyama, Y. Inoue, Photocatalytic activity for water decomposition of RuO_2-dispersed Zn_2GeO_4 with d^{10} configuration, J. Phys. Chem. B 108 (2004) 4369–4375, https://doi.org/10.1002/chin.200427016.

[12] C. Yan, P. Lee, Synthesis and structure characterization of ternary Zn_2GeO_4 nanowires by chemical vapor transport, J. Phys. Chem. C 113 (2009) 14135–14139, https://doi.org/10.1021/jp9050879.

[13] Y. Wang, M. Zheng, H. Zhao, H. Qin, W. Fan, X. Zhao, Zn_2GeO_{4-x}/ZnS heterojunctions fabricated via in situ etching sulfurization for Pt-free photocatalytic hydrogen evolution: interface roughness and defect engineering, Phys. Chem. Chem. Phys. 22 (2020) 10265–10277, https://doi.org/10.1039/D0CP01308K.

[14] Q. Kang, T. Wang, P. Li, L. Liu, K. Chang, M. Li, J. Ye, Photocatalytic reduction of carbon dioxide by hydrous hydrazine over Au-Cu alloy nanoparticles supported on $SrTiO_3$/TiO_2 coaxial nanotube arrays, Angew. Chem. Int. Ed. 127 (2014) 855–859, https://doi.org/10.1002/ange.201409183.

[15] K. Maeda, K. Teramura, D. Lu, N. Saito, Y. Inoue, K. Domen, Roles of Rh/Cr_2O_3 (core/shell) nanoparticles photodeposited on visible-light-responsive $(Ga_{1-x}Zn_x)(N_{1-x}O_x)$ solid solutions in photocatalytic overall water splitting, J. Phys. Chem. C 111 (2007) 7554–7560, https://doi.org/10.1021/jp071056j.

[16] M. Muñoz-Batista, D. Meira, G. Colón, A. Kubacka, M. Fernández-García, Phase-contact engineering in mono- and bimetallic cu-Ni co-catalysts for hydrogen photocatalytic materials, Angew. Chem. Int. Ed. 57 (2018) 1199–1203, https://doi.org/10.1002/anie.201709552.

[17] Y. Wang, Y. Zhang, X. Xin, J. Yang, M. Wang, R. Wang, P. Guo, W. Huang, A.J. Sobrido, X. Li, In situ photocatalytically enhanced thermogalvanic cells for electricity and hydrogen production, Science 381 (2023) 291–296, https://doi.org/10.1126/science.adg0164.

[18] Y. Zhang, Y. Li, X. Xin, Y. Wang, P. Guo, R. Wang, B. Wang, W. Huang, A.J. Sobrido, X. Li, Internal quantum efficiency higher than 100% achieved by combining doping and quantum effects for photocatalytic overall water splitting, Nat. Energy 8 (2023) 504–514, https://doi.org/10.1038/s41560-023-01242-7.

[19] Q. Liu, Q. Chen, T. Li, Q. Ren, S. Zhong, Y. Zhao, S. Bai, Vacancy engineering of AuCu cocatalysts for improving the photocatalytic conversion of CO_2 to CH_4, J. Mater. Chem. A 7 (2019) 27007–27015, https://doi.org/10.1039/C9TA09938G.

[20] J. Wen, J. Xie, H. Zhang, A. Zhang, Y. Liu, X. Chen, X. Li, Constructing multifunctional metallic Ni interface layers in the g-C_3N_4 nanosheets/amorphous NiS heterojunctions for efficient photocatalytic H_2 generation, ACS Appl. Mater. Interfaces 9 (2017) 14031–14042, https://doi.org/10.1021/acsami.7b02701.

[21] W. Zhou, Z. Yin, Y. Du, X. Huang, Z. Zeng, Z. Fan, H. Liu, J. Wang, H. Zhang, Synthesis of few-layer MoS_2 nanosheet-coated TiO_2 nanobelt heterostructures for enhanced photocatalytic activities, Small 9 (2013) 140–147, https://doi.org/10.1002/smll.201201161.

[22] K. Zhang, J. Kim, B. Park, S. Qi, B. Ji, X. Sheng, H. Zeng, H. Shin, S. Oh, C. Lee, J. Park, Defect-induced epitaxial growth for efficient solar hydrogen production, Nano Lett. 17 (2017) 6676–6683, https://doi.org/10.1021/acs.nanolett.7b02622.

[23] Z. Hou, X. Zou, X. Song, X. Pu, Y. Geng, L. Wang, Fabrication of CdS/Zn_2GeO_4 heterojunction with enhanced visible-light photocatalytic H_2 evolution activity, Int. J. Hydrogen Energy 44 (2019) 28649–28655, https://doi.org/10.1016/j.ijhydene.2019.08.232.

[24] Z. Hou, X. Zou, X. Pu, L. Wang, Y. Geng, Facile synthesis and improved photocatalytic H_2 production of ZnO/Zn_2GeO_4 and ZnO/Zn_2GeO_4-Cu composites, J. Solid State Chem. 296 (2021) 121965, https://doi.org/10.1016/j.jssc.2021.121965.

[25] S. Chen, S. Shen, G. Liu, Y. Qi, F. Zhang, C. Li, Interface engineering of a CoO_x/Ta_3N_5 photocatalyst for unprecedented water oxidation performance under visible-light-irradiation, Angew. Chem. Int. Ed. 54 (2015) 3047–3051, https://doi.org/10.1002/anie.201409906.

[26] K. Chang, X. Hai, H. Pang, H. Zhang, L. Shi, G. Liu, H. Liu, G. Zhao, M. Li, J. Ye, Targeted synthesis of 2H- and 1T-Phase MoS_2 monolayers for catalytic hydrogen evolution, Adv. Mater. 28 (2016) 10033–10041, https://doi.org/10.1002/adma.201603765.

[27] Y. Li, J. Xing, Z. Chen, Z. Li, F. Tian, L. Zheng, H. Wang, P. Hu, H. Zhao, H. Yang, Unidirectional suppression of hydrogen oxidation on oxidized platinum clusters, Nat. Commun. 4 (2013) 2500, https://doi.org/10.1038/ncomms3500.
[28] D. Kim, T. Yoon, Y. Jang, J. Lee, Y. Na, B. Lee, J. Lee, K. Kim, Band gap narrowing of zinc orthogermanate by dimensional and defect modification, J. Phys. Chem. C 123 (2019) 14573–14587, https://doi.org/10.1021/acs.jpcc.9b03728.
[29] B. Ma, F. Wen, H. Jiang, J. Yang, P. Ying, C. Li, The synergistic effects of two co-catalysts on Zn_2GeO_4 on photocatalytic water splitting, Catal. Lett. 134 (2010) 78–86, https://doi.org/10.1007/s10562-009-0220-8.
[30] A. Sunny, K. Balasubramanian, Laser-induced phonon and magnon properties of NiO nanoparticles: a Raman study, J. Raman Spectrosc. 52 (2021) 833–842, https://doi.org/10.1002/jrs.6067.
[31] M. Rahman, M. Kibria, C. Mullins, Metal-free photocatalysts for hydrogen evolution, Chem. Soc. Rev. 49 (2020) 1887, https://doi.org/10.1039/C9CS00313D.
[32] X. Tao, Y. Zhao, S. Wang, C. Li, R. Li, Recent advances and perspectives for solar-driven water splitting using particulate photocatalysts, Chem. Soc. Rev. 51 (2022) 3561–3608, https://doi.org/10.1039/D1CS01182K.
[33] J. He, P. Liu, R. Ran, W. Wang, W. Zhou, Z. Shao, Single-atom catalysts for high-efficiency photocatalytic and photoelectrochemical water splitting: distinctive roles, unique fabrication methods and specific design strategies, J. Mater. Chem. A 10 (2022) 6835–6871, https://doi.org/10.1039/D2TA00835A.
[34] Z. Wang, C. Li, K. Domen, Recent developments in heterogeneous photocatalysts for solar-driven overall water splitting, Chem. Soc. Rev. 48 (2019) 2109–2125, https://doi.org/10.1039/C8CS00542G.